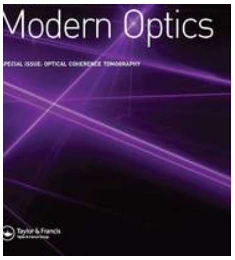

Journal of Modern Optics

ISSN: 0950-0340 (Print) 1362-3044 (Online) Journal homepage: http://www.tandfonline.com/loi/tmop20

Position and rotation-invariant pattern recognition system by binary rings masks

S. Solorza & J. Álvarez-Borrego

Journal of Modern Optics, 2015
Vol. 62, No. 10, 851–864, http://dx.doi.org/10.1080/09500340.2015.1013579

Position and rotation-invariant pattern recognition system by binary rings masks

S. Solorza[a*] and J. Álvarez-Borrego[b]

[a]*Facultad de Ciencias, Matemáticas Aplicadas, UABC, Ensenada, Mexico;* [b]*División de Física Aplicada, Departamento de Óptica, Centro de Investigación Científica y de Educación Superior de Ensenada, Ensenada, Mexico*

(*Received 3 October 2014; accepted 26 January 2015*)

In this paper, algorithms invariant to position, rotation, noise and non-homogeneous illumination are presented. Here, several manners are studied to generate binary rings mask filters and the corresponding signatures associated to each image. Also, in this work it is shown that digital systems, which are based on the k-law non-linear correlation, are k-invariant for $0 < k < 1$. The methodologies are tested using greyscale fossil diatoms digital images (real images), and considering the great similarity between those images the results obtained are excellent. The box plot statistical analysis and the computational cost times yield that the Bessel rings masks are the best option when the images contain a homogeneous illumination and the Fourier masks digital system is the right selection when the non-homogeneous illumination and noise is presented in the images.

Keywords: image processing; pattern recognition; digital systems; binary rings masks; one-dimensional signatures

1. Introduction

One of the goals in the pattern recognition field is to recognize objects automatically with a high level of confidence and a low cost of computational time; it does not matter if the objects are rotated, scaled, displaced, with different kind of noise, different illumination or perhaps they are partially hidden or we have a fragment of it only. The design of new filters for pattern recognition based on correlation has attracted considerable attention [1–10]; most of these filters have been used to recognize micro and macro structures.

Recently, a new methodology based on one-dimensional signatures of the images was presented [9,10]. In these works, shift and rotation were taken into account in the correlation process and different ways to generate the binary rings masks were studied. In this paper, we showed more alternatives to generate the binary rings masks; moreover, illumination and noise variations in the objects to be recognized were analysed. Also, the independence of the system in the non-linear factor k is determined. Finally, here is established the robust algorithm based on binary rings masks that uses lesser computational time.

Because the goal of these systems is to be used in the classification of digital images taken from the life, that is, digital images not generated by computers, therefore the objects used in this paper are microstructures called diatoms (real images). The diatom samples are from Cuenca de San Lázaro in Baja California and they were taken in 1996 in an oceanographic ship called El PUMA [11]. Fossil diatoms are photosynthetic organisms that live in freshwater or marine and they constitute a very important part of the phytoplanktons. The presence of diatom valves in marine paleoenvironments has been used for studying the climatic changes as well as geomorphological processes [12,13]. The identification of diatom fossils requires the analysis of a great number of valves per sample. Generally, to obtain relative abundances and diversity indexes, diatom counts must go from 400 to 10^7 structures per gram [14]. Thus, the analysis of these samples requires the investment of much time and experience. Moreover, these kinds of images are one of the best options to test the efficiency of the pattern recognition digital system because a lot of them are morphologically similar.

The material in this work is organized as follows: in Section 2, the digital system invariant to position and rotation based on the Fourier binary rings masks is explained. Section 3 presents the digital system by the Bessel binary rings masks. Section 4 shows the comparison analysis of the methodologies in Sections 2 and 3, and that given in [15] called vectorial signatures. The confidence level of each of those methodologies, the computational time, noise and the non-homogeneous illumination analysis are presented. Finally, in Section 5 the conclusions are given.

*Corresponding author. Email: selene.solorza@uabc.edu.mx

2. Digital system by the Fourier binary rings masks

The digital system works with $n \times n$ greyscale images only. For a given image I, (x, y) represent a pixel of the image and $I(x, y)$ its corresponding intensity value, $x, y \in \{1, \ldots, n\}$ and the centred pixel (c_x, c_x) of the image is given by

$$c_x = \begin{cases} \frac{n}{2} + 1, & \text{if } n \text{ is even}, \\ \lfloor \frac{n}{2} \rfloor + 1, & \text{if } n \text{ is odd}, \end{cases} \tag{1}$$

here $\lfloor z \rfloor$ rounds z to the nearest integer towards $-\infty$. In Figure 1(a), $n = 307$ and $c_x = 154$.

2.1. The Fourier binary rings masks

The masks of a selected image I can be built by taking the real and imaginary parts of its Fourier transform, that is, $\mathrm{Re}(FT(I))$ and $\mathrm{Im}(FT(I))$, Figure 1(b) and (c), respectively.

The binary disk mask D is defined like,

$$D = \begin{cases} 1, & \text{if } d\left((c_x, c_x), (x, y)\right) \leq n, \\ 0, & \text{otherwise}, \end{cases} \tag{2}$$

where $x, y \in \{1, \ldots, n\}$ and $d(p, q)$ is the Euclidean distance between p and q points, thus the D image is centered in the (c_x, c_x) pixel and has a diameter of n-pixels. Figure 1(d) presents a disk filter of diameter 307.

The binary disk mask D is used to filter the image $\mathrm{Re}(FT(I))$ as it is shown in Figure 1(e). Also, the image $\mathrm{Im}(FT(I))$ is filtered by D (Figure 1(f)). Mathematically, those operations are given by

$$f_R = D * \mathrm{Re}(FT(I)), \tag{3}$$

$$f_I = D * \mathrm{Im}(FT(I)), \tag{4}$$

where $*$ means an element-wise product or Hadamard product. From the f_R image, 180 profiles were obtained, sampling the entire circle. The profiles are n-pixels length and the (c_x, c_x) pixel is a common point of all of them. Analogously for f_I image. Figure 1(e) and (f) show the zero-degree profiles P_R^0 and P_I^0 and the discontinuous black lines represent some profiles separated $\Delta\theta = 20°$ from each other. In general, the profile equations are expressed as

$$P_R^\theta(x) = f_R\left(x, y(x)\right), \tag{5}$$

$$P_I^\theta(x) = f_I\left(x, y(x)\right), \tag{6}$$

where $x = 1, \ldots, n$, $y(x) = m(x - x_1) + y_1$, m is the slope of y, $(x_1, y_1) = (c_x + c_x \cos\theta, c_x - c_x \sin\theta)$ and $(x_2, y_2) = (c_x + c_x \cos(\theta + \pi), c_x - c_x \sin(\theta + \pi))$ are the two distinct end points of that line segment and θ is the angle that y has in respect to the horizontal axis in the Cartesian plane (considering that the origin $(0, 0)$ of the Cartesian plane is set at the centre pixel of the image (c_x, c_x)), and sampling is performed in this manner for the entire disc. Next, the addition of the squared intensity values in each profile is computed, that is,

$$s_R^\theta = \sum_{x=1}^{n} \left(P_R^\theta(x)\right)^2, \tag{7}$$

$$s_I^\theta = \sum_{x=1}^{n} \left(P_I^\theta(x)\right)^2, \tag{8}$$

and the profile whose sum has the maximum value will be selected,

$$\alpha_\beta = \max_{0 \leq \theta \leq 179} \{s_R^\theta\}, \quad T_R = P_R^\beta, \tag{9}$$

$$\alpha_\gamma = \max_{0 \leq \theta \leq 179} \{s_I^\theta\}, \quad T_I = P_I^\gamma, \tag{10}$$

where β and γ are the angles of the profiles in f_R and f_I whose sum has the maximum value. T_R and T_I are called the maximum energy profiles. For example, Figure 1(e) shows the maximum energy profile for the real part of the Fourier transform of the image in Figure 1(a), this profile (T_R) is shown in the Cartesian plane in Figure 1(g). Figure 1(f) gives the maximum energy profile for the imaginary part of the Fourier transform of the image in Figure 1(a) and its representation in the Cartesian plane is shown in Figure 1(h).

Based on Equation (9), the two binary functions can be built,

$$Z_{RP}(x) = \begin{cases} 1, & \text{if } T_R(x) > 0, \\ 0, & \text{if } T_R(x) \leq 0, \end{cases} \tag{11}$$

$$Z_{RN}(x) = \begin{cases} 0, & \text{if } T_R(x) > 0, \\ 1, & \text{if } T_R(x) \leq 0, \end{cases} \tag{12}$$

where $x = 1, \ldots, n$. Analogously, from Equation (10) the two binary functions obtained are,

$$Z_{IP}(x) = \begin{cases} 1, & \text{if } T_I(x) > 0, \\ 0, & \text{if } T_I(x) \leq 0, \end{cases} \tag{13}$$

$$Z_{IN}(x) = \begin{cases} 0, & \text{if } T_I(x) > 0, \\ 1, & \text{if } T_I(x) \leq 0, \end{cases} \tag{14}$$

the first sub-index in Equations (11)–(14) indicates if the profile comes from the real (R) or the imaginary (I) part of the Fourier transform of the image. The second sub-index P means that the positive values of the profile are taken and N represents that the non-positive values are considered. Finally, taking the vertical axis $x = 154$ as the rotation axis, the right branch of the graphs of Z_{RP}, Z_{RN}, Z_{IP} and Z_{IN} are rotated 180° to obtain concentric cylinders of one height, different widths and centred in (c_x, c_x) pixel [9,10]. Taking a cross-section of those cylinders, the binary rings masks associated to the given image are realised. Following the sub-index notation, the binary rings masks are named as, M_{RP}, M_{RN}, M_{IP} and M_{IN}. Figure 2 shows the masks associated to the image in Figure 1(a).

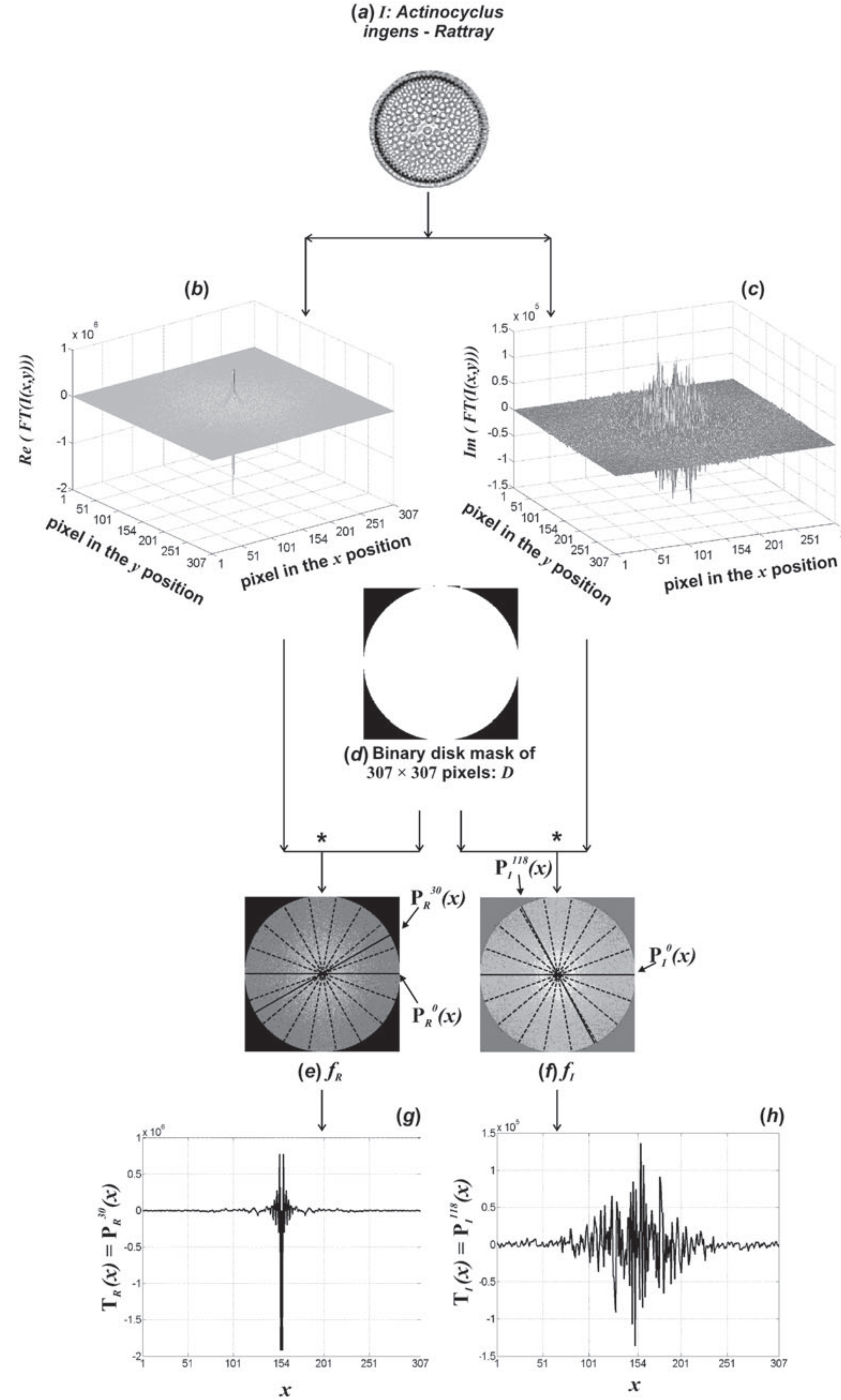

Figure 1. Procedure to obtain the maximum energy profiles. The ∗ means an element-wise product or Hadamard product. Only for visualization purposes (*e*) and (*f*) figures are shown in log scale.

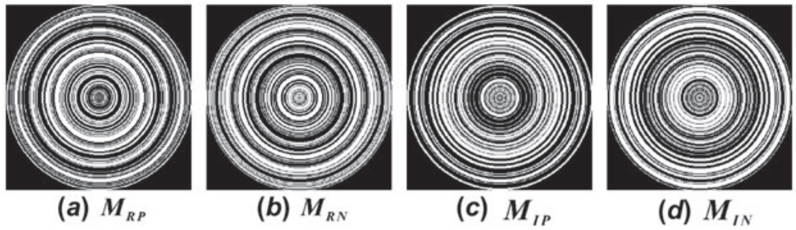

Figure 2. The Fourier binary rings masks associated to the image in Figure 1(a).

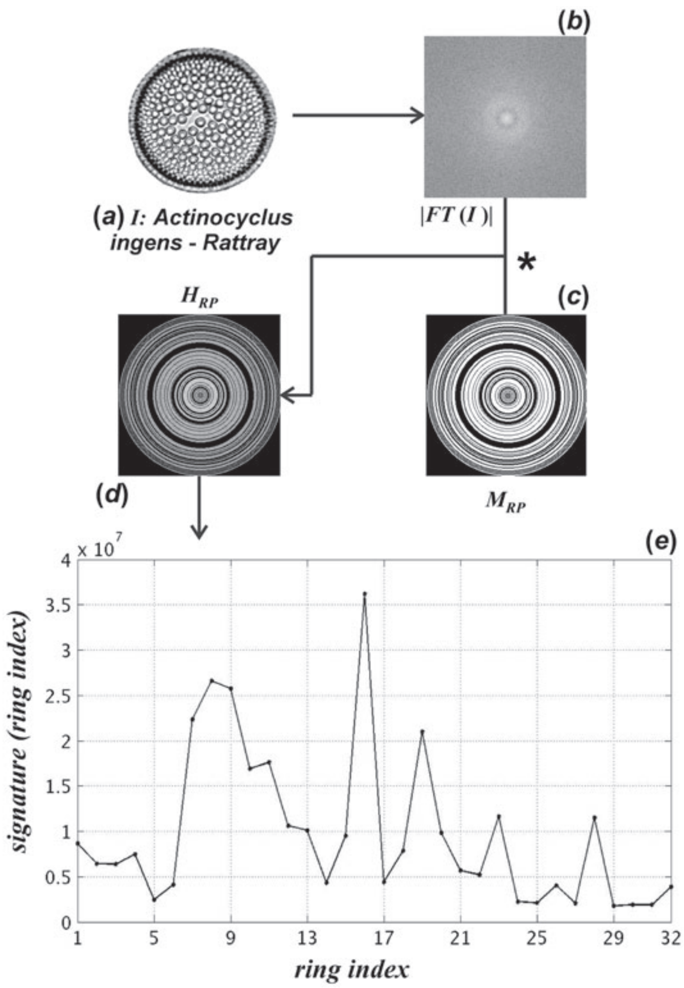

Figure 3. Signature example procedure. The $*$ means an element-wise product. Only for visualization purposes the (b) and (d) figures are shown in log scale.

2.2. *The one-dimensional signatures*

The digital system uses the modulus of the Fourier transform of the image, $|FT(I)|$, because it is invariant to translation, that is, $|FT(I(x, y)) = FT(I(x+\tau, y+\zeta))|$, where $\tau, \zeta \in \mathbb{R}$, hence the system is invariant to translation.

To obtain the invariant to rotation, one-dimensional (1D) signatures based on binary rings masks are built. The first step in the signature construction is to filter the modulus of the Fourier transform of the image by the binary rings masks. For example, the amplitude spectrum (Figure 3(b)) of Figure 3(a) is filtered by the binary rings mask M_{RP} (Figure 3(c)) as

$$H_{RP} = M_{RP} * |FT(I)|. \tag{15}$$

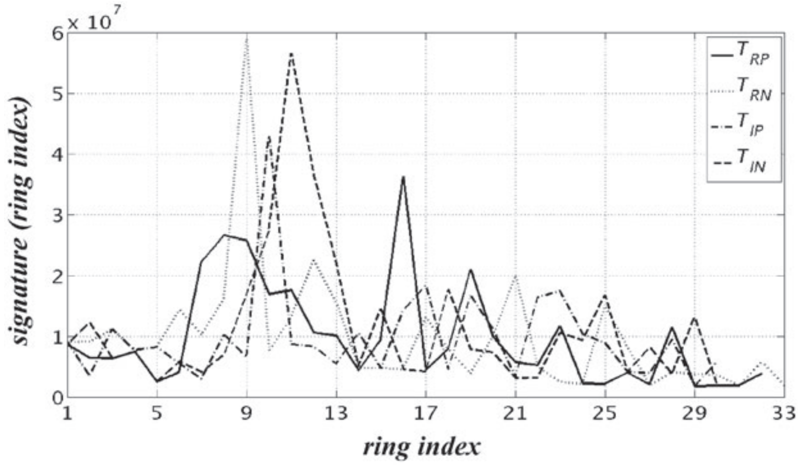

Figure 4. The signatures associated to image in Figure 3(*a*).

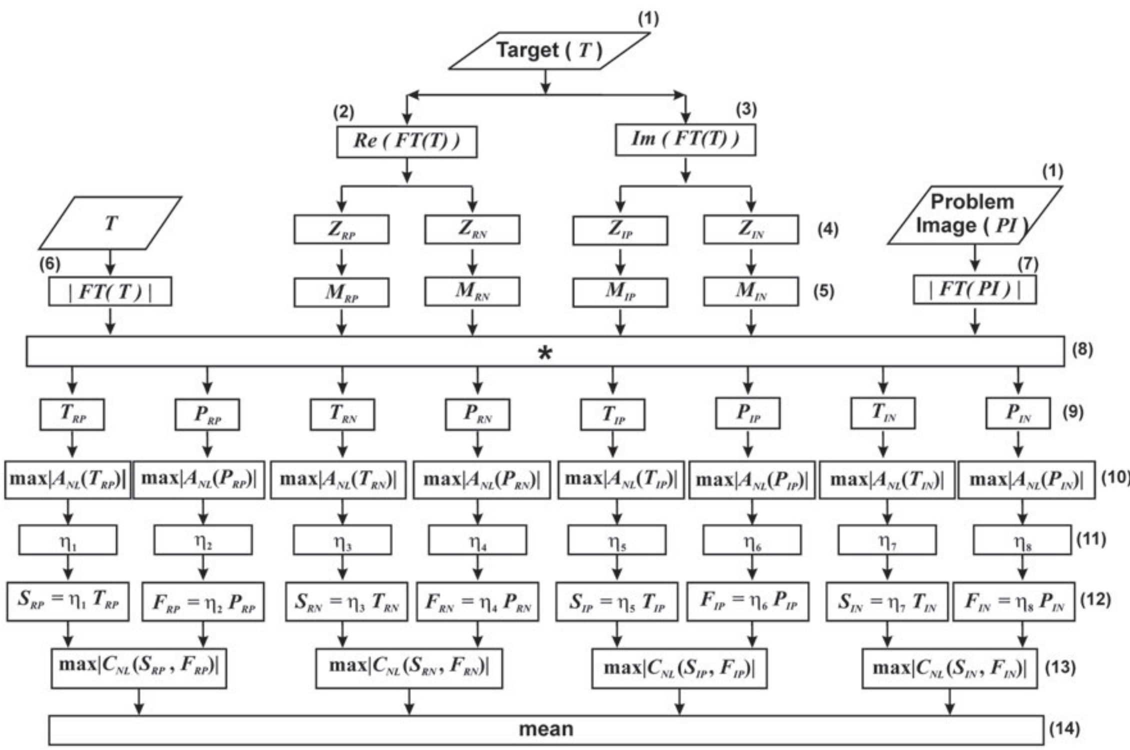

Figure 5. Algorithm for the digital system by the Fourier binary rings masks.

The result of Equation (15) is presented in Figure 3(*d*). The rings in H_{RP} are numbered from the centre towards outside to obtain the following set,

$$\text{Index} = \{\text{ring index} \in \bar{n}\}, \tag{16}$$

where $\bar{n} = \{1, \ldots, n\}$. The addition of the intensity values in each ring in the image H_{RP} are calculated to build the function

$$\begin{aligned} &\text{signature} = \text{Index} \;\rightarrow A \subset \mathbb{R}, \\ &\text{signature(ring index)} \\ &\quad = \sum H_{RP}(x, y), \\ &\qquad \text{if } H_{RP}(x, y) \text{ belongs to ring index.} \end{aligned} \tag{17}$$

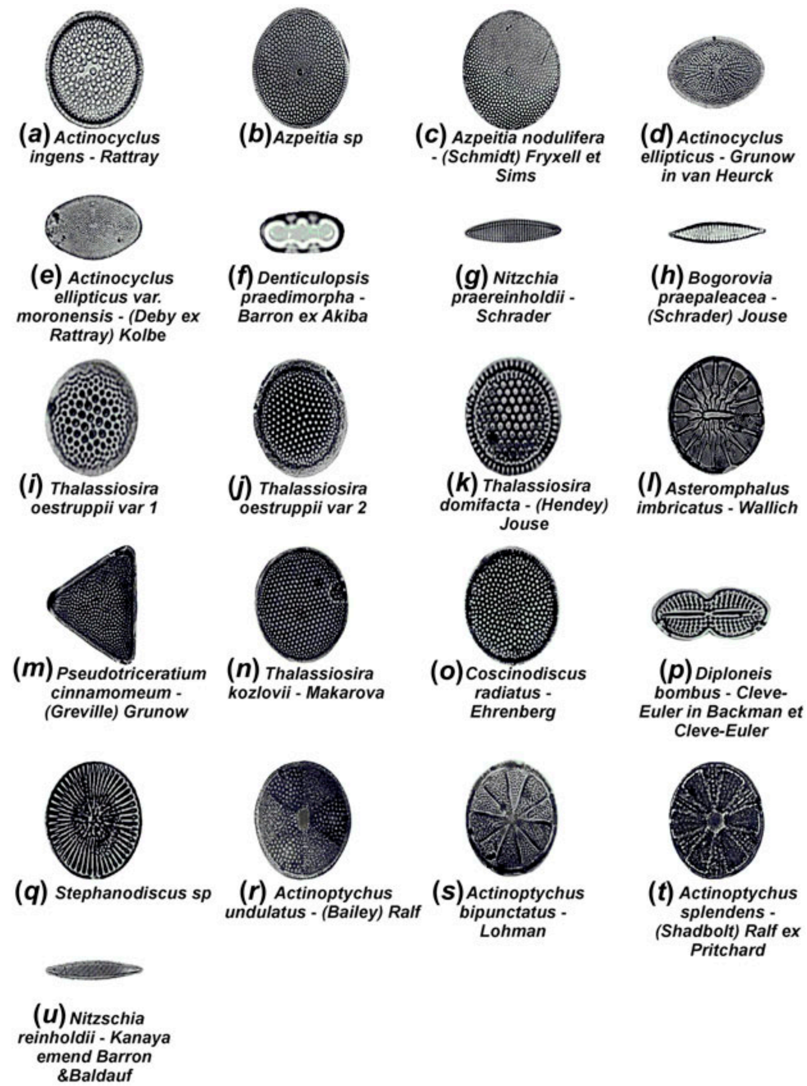

Figure 6. Database of 21 diatoms. (The color version of this figure is included in the online version of the journal.)

Because the cardinality of A is bigger than one, the graph of the signature function is called 1D signature of the image I. When the cardinality of A is one, then we have a scalar signature of I. Figure 3(e) shows the 1D signature constructed by the binary rings mask M_{RP}, hence it is named T_{RP}. Analogously, T_{RN}, T_{IP} and T_{IN} are obtained using M_{RN}, M_{IP} and M_{IN}, respectively. Figure 4 presents the four signatures of the image in Figure 3(a). Because the number of rings in each mask is different then, the length of the signature is also different.

2.3. The digital system procedure

In Figure 5 the algorithm of the digital correlation system invariant to position and rotation is given. In the first step, the target and problem images are chosen. After that, the real and imaginary parts of the Fourier transform of the target are obtained, respectively, in steps 2 and 3. In step 4, the binary profiles based on Equations (11)–(14) are computed. Next, the Fourier binary rings masks are built (step 5). Thereafter, the modulus of the Fourier transform of the target ($|FT(T)|$) and the problem image ($|FT(PI)|$) are given (steps 6 and 7). Then, both images ($|FT(T)|$ and $|FT(PI)|$) are filtered by the binary rings masks M_{RP}, M_{RN}, M_{IP} and M_{IN} (step 8). In step 9, eight signatures are obtained following the procedure described in Section 2.2; here T represents the signatures that come from the target and P is for those associated to the problem image, and the sub-index follows the nomenclature of the corresponding masks used to construct the signature. To obtain an efficient digital system, each signature will be weighted by their scalar factor (step 11), given by

$$\eta_S = \max |A_{NL}(S)|, \tag{18}$$

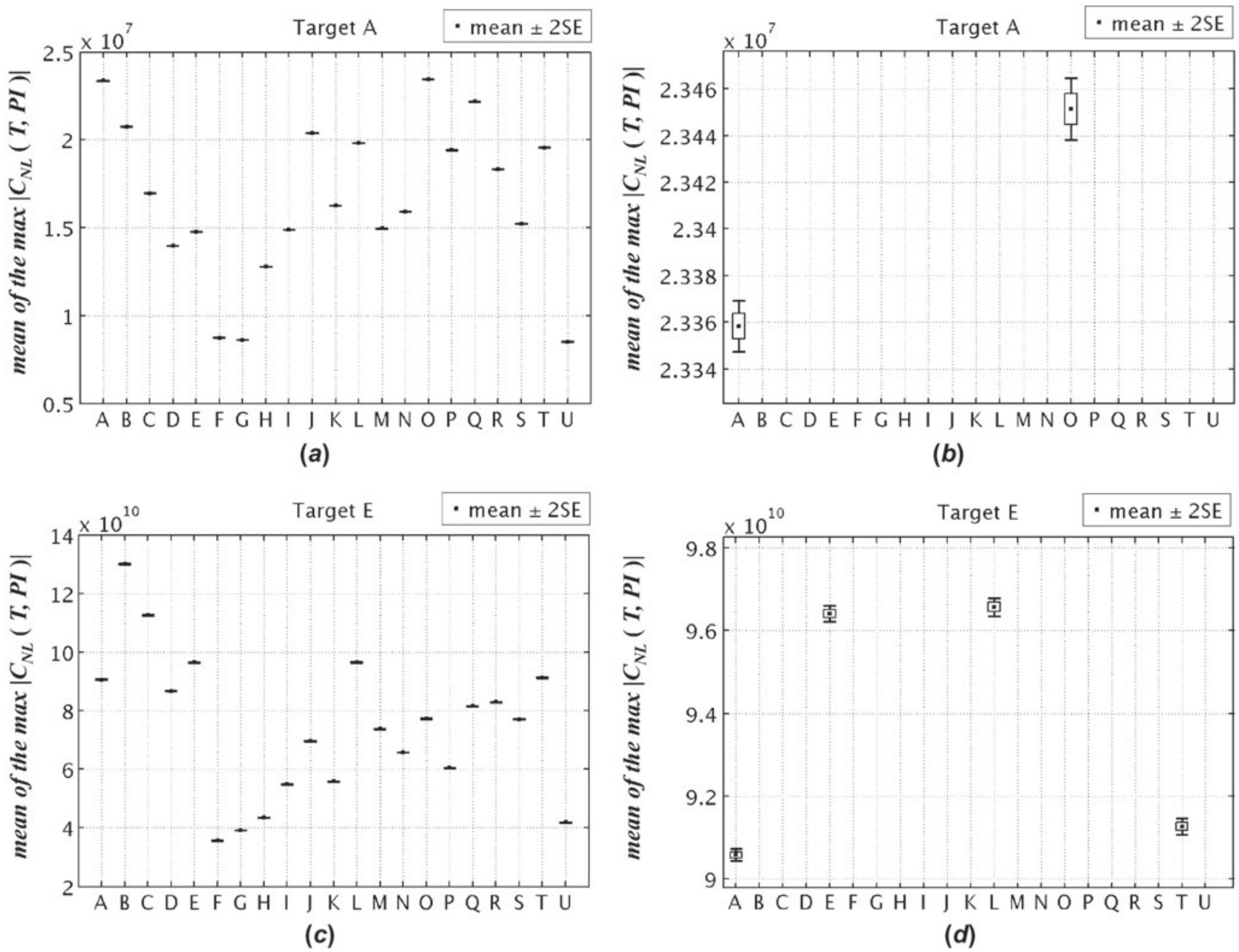

Figure 7. T and PI represent the signatures of the target and the problem image, respectively. (*a*) The box plot for the mean of the maximum values of the non-linear correlation using target A and $k = 0.3$. (*b*) Amplification around the zone of target A. (*c*) The box plot for the mean of the maximum values of the non-linear correlation using target E and $k = 0.4$. (*d*) Amplification around the zone of target E.

which comes from the non-linear autocorrelation

$$A_{NL}(S) = |FT^{-1}\left(\left|FT(S)|^k\, e^{i\varphi}\, |FT(S)|^k\, e^{-i\varphi}\right)\right|, \tag{19}$$

where $S = T_{RP}, T_{RN}, T_{IP}, T_{IN}, P_{RP}, P_{RN}, P_{IP}$ and P_{IN}, and φ is the phase of the Fourier transform of the signature and $0 < k < 1$ is the non-linear coefficient (step 10).

Once, each signature is weighted (step 12) and named S_j for the target and F_j for the problem image ($j = RP$, RN and IP or IN), the non-linear correlation of the signatures is computed as

$$C_{NL}(S_j, F_j) = FT^{-1}\left(|FT(F_j)|^k\, e^{i\phi}\, |FT(S_j)|^k\, e^{-i\varphi}\right), \tag{20}$$

where φ and ϕ are the phases of the Fourier transform of the signatures for the target and the problem image, respectively. In step 13, the maximum values of the magnitude for the four correlations are obtained to get the mean of these values (step 14). If the mean value of the problem image is similar to the mean value of the target ($PI \approx T$), then the problem image is the same as the target, otherwise they are different.

2.4. Results

The algorithm in Figure 5 was tested using the 307 × 307 greyscale diatom digital images shown in Figure 6. Each image was selected as target, thus the target database has 21 elements. The target images were rotated 360°, one degree by one degree, until the circle was completed; hence, in the problem images database 7,560 images were processed.

Table 1. Confidence level (in %) of the digital system by Fourier masks.

Diatom	$k_{0.1}$	$k_{0.2}$	$k_{0.3}$	$k_{0.4}$	$k_{0.5}$	$k_{0.6}$	$k_{0.7}$	$k_{0.8}$	$k_{0.9}$
A	95.4	95.4	95.4	95.4	95.4	95.4	95.4	95.4	95.4
B	95.4	95.4	95.4	95.4	95.4	95.4	95.4	95.4	95.4
C	95.4	95.4	95.4	95.4	95.4	95.4	95.4	95.4	95.4
D	95.4	95.4	95.4	95.4	95.4	95.4	95.4	95.4	68.3 d/R
E	95.4	95.4	95.4	95.4 w/L	95.4	95.4	95.4	95.4	68.3 d/N
F	95.4	95.4	95.4	95.4	95.4	95.4	95.4	95.4	95.4
G	95.4	95.4	95.4	95.4	95.4	95.4	95.4	95.4	95.4
H	95.4	95.4	95.4	95.4	95.4	95.4	95.4	95.4	95.4
I	95.4	95.4	95.4	95.4	95.4	95.4	95.4	95.4	68.3 d/P
J	95.4	95.4	95.4	95.4	95.4	95.4	95.4	95.4	95.4
K	95.4	95.4	95.4	95.4	95.4	95.4	95.4	95.4	95.4
L	95.4	95.4	95.4	95.4	95.4	95.4	95.4	95.4	95.4
M	95.4	95.4	95.4	95.4	95.4	95.4	95.4	95.4	95.4
N	95.4	95.4	95.4	95.4	95.4	95.4	95.4	95.4	95.4
O	95.4	95.4	95.4	95.4	95.4	95.4	95.4	95.4	95.4
P	95.4	95.4	95.4	95.4	95.4	95.4 w/K	95.4	95.4	95.4
Q	95.4	95.4	95.4	95.4	95.4	95.4	95.4	95.4	95.4
R	95.4	95.4	95.4	95.4	95.4	95.4	95.4	95.4	95.4
S	95.4	95.4	95.4	95.4	95.4	95.4	95.4	95.4	95.4
T	95.4	95.4	95.4	95.4	95.4	95.4	95.4	95.4	95.4
U	95.4	95.4	95.4	95.4	95.4	95.4	95.4	95.4	95.4

Table 2. Computational time ranking from the lowest (1) to the highest (15) of the digital systems based on the Fourier binary rings masks.

#	Masks	Confidence level %
1	$M_{RP}, M_{RN}, M_{IP}, M_{IN}$	95.4
2	M_{RP}, M_{IP}, M_{IN}	95.4
3	M_{RP}, M_{RN}	95.4
4	M_{RN}	95.4
5	M_{RN}, M_{IP}	95.4
6	M_{RP}, M_{IP}	95.4
7	M_{RP}, M_{RN}, M_{IP}	95.4
8	M_{RP}, M_{RN}, M_{IN}	95.4
9	M_{IP}, M_{IN}	95.4
10	M_{RN}, M_{IP}, M_{IN}	95.4
11	M_{RP}, M_{IN}	95.4
12	M_{IP}	95.4
13	M_{RN}, M_{IN}	95.4
14	M_{RP}	95.4
15	M_{IN}	95.4

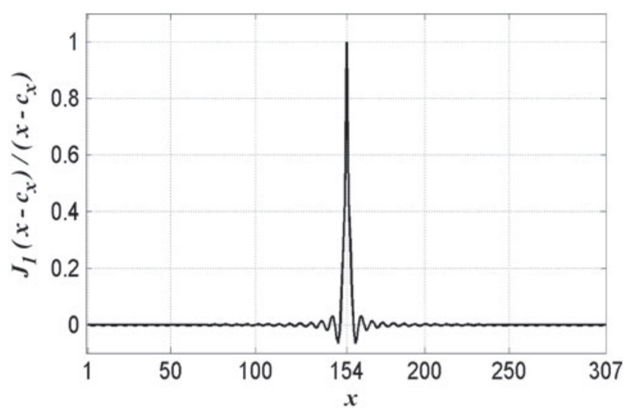

Figure 8. The graph of the ratio of the Bessel function of first kind and first order by its argument. Here, the function is defined as one when $x = c_x$.

Moreover, due to the rotation of the images, the saw-tooth effect (noise) is taken into account, thus the digital system is more robust for the pattern recognition problem. The average maximum values of the magnitude for the non-linear correlations is box plotting using the mean of those average values with two standard errors ($\pm 2SE$). Figure 7(a) shows an example of a box plot when the diatom A is the target and $k = 0.3$ was used in Equation (20). There is not an overlap of the whiskers (Figure 7(b)), hence it can be concluded that the system has a confidence level at least of 95.4% to identify diatoms A.

The result of the statistical analysis of the system is presented in Table 1, the confidence level is given in percentage and the notation of 68.3% d/X means that the system has a confidence level of 68.3% due to image X, and 95.4 w/X means that the system has a confidence level of 95.4% without considering image X. Also, in Table 1 the results of the study of the non-linear factor k in Equation (20) are given. As it is expected, as k goes to one, the confidence level decreases, that is, the non-linear equation approaches to the linear limit. Based on Table 1, it can be concluded that the system works excellently for $0 < k < 1$ because the non-linear equation is non-commutative, that means for example if $k = 0.4$, the system using diatom

E as target will name erroneously some diatoms L as E (Figure 7(*c*) and (*d*)). But the system identified diatoms L without mistakes; then all the images that the system classified as diatoms E, will be tested again using the diatom L as the target, hence the system will identify without doubt the diatoms L and the rest are diatoms E, therefore the complete identification is done, but it will use more computational-time. The same idea works for the other cases presented in Table 1. Furthermore, the digital system was tested using all arrangements of the four masks, obtaining basically that the system has a confidence level at least of 95.4% and it is independent of the non-linear factor k. From this analysis, it can be concluded that when the four masks are used, the digital system presents less computational cost time, which is the algorithm given in Figure 5. Table 2 gives the ranking in time performance (from the lowest, 1, to the highest, 9) for all combinations of the four masks. Also, studies were done without weighting the signatures, but the system presents a confidence level lower than those given weighting the signatures.

3. The digital system by Bessel masks

Now, an easier digital system of binary rings mask will be build. To make it, the ratio of the Bessel function of first kind and first order by its argument is taken, that is

$$f(x) = \begin{cases} \frac{J_1(x-c_x)}{x-c_x}, & 1 \leq x \neq c_x \leq n, \\ 1, & x = c_x, \end{cases} \tag{21}$$

where c_x is given in Equation (1). As shown in Figure 8, f is centred at c_x, it is symmetric and its x-axis length is $n = 307$. As in the case of the binary rings masks construction in Section 2.1, here there are two choices to build the binary function

$$Z_P(x) = \begin{cases} 1, & \text{if } f(x) > 0, \\ 0, & \text{if } f(x) \leq 0, \end{cases} \tag{22}$$

$$Z_N(x) = \begin{cases} 0, & \text{if } f(x) > 0, \\ 1, & \text{if } f(x) \leq 0. \end{cases}$$

After rotating 180 degrees the right branch of the graphs of Z_P and Z_N, the binary rings masks B_P and B_N are obtained. Once the masks are set, the signatures associated to a given image I are computed as in Section 2.2, but instead of using M_{RP}, M_{RN}, M_{IP} and M_{IN} masks here we used B_P and B_N as nomenclature.

3.1. *The digital system*

Figure 9 shows the procedure for the algorithm invariant to position and rotation using Bessel masks. In this method, the target and the problem image are selected (step 1). Then, the moduli of the Fourier transform of the images are obtained (step 2). The decision, in step 3, will be taken to build the binary mask of concentric circular rings. In step 4, after choosing one of the two options, the Bessel mask is constructed. In step 5, the mask is applied to the $|FT(T)|$ and $|FT(PI)|$. Next, the signature of the problem and the target images is obtained (step 6). Finally, if the maximum value of the magnitude for the non-linear correlation, Equation (20), is significant, the PI contains the target; otherwise, it has a different object to the target (step 7).

3.2. *Results*

Table 3, shows the results of the digital system in Figure 9 using the Bessel mask B_{NP}, the first sub-index would indicate whether the signatures are weighted by the maximum of the non-linear autocorrelation value (W) or not (N), the second sub-index indicates if Equation (22) is taken, that is the positive values in the profile (P) or the non-positive values (N) are considered, Equation (**??**). The confidence level is given in percentage and the notation 68.3% d/X

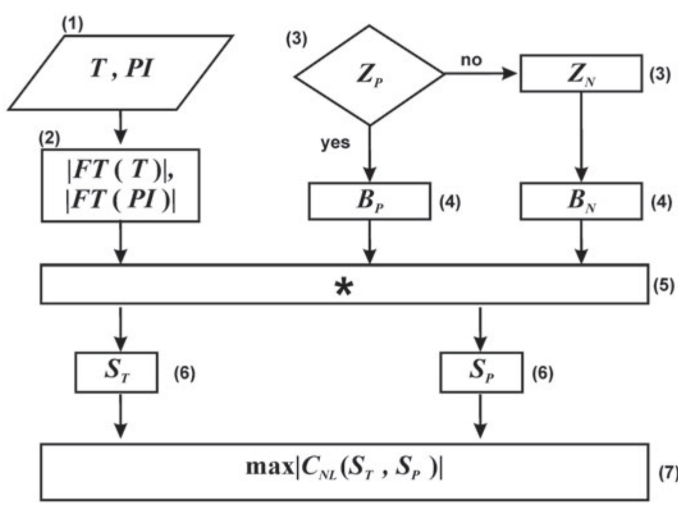

Figure 9. Algorithm for the digital system of Bessel masks.

Table 3. Confidence level (in %) of the digital system by B_{NP} mask.

Diatom	$k_{0.1}$	$k_{0.2}$	$k_{0.3}$	$k_{0.4}$	$k_{0.5}$	$k_{0.6}$	$k_{0.7}$	$k_{0.8}$	$k_{0.9}$
A	95.4	95.4	95.4	95.4	95.4	95.4	95.4	95.4	95.4
B	95.4	95.4	95.4	95.4	95.4	95.4	95.4	95.4	95.4
C	95.4	95.4	95.4	95.4	95.4	95.4	95.4	95.4	95.4
D	95.4	95.4	95.4	68.3 d/B	95.4	95.4	95.4	95.4	95.4
E	95.4	95.4	95.4	95.4	68.3 d/T	68.3 d/L	95.4	95.4	95.4
F	95.4	95.4	95.4	95.4	95.4	95.4	95.4	95.4	95.4
G	95.4	95.4	95.4	95.4	95.4	95.4	95.4	95.4	95.4
H	95.4	95.4	95.4	95.4	95.4	95.4	68.3 d/C,D	95.4	95.4
I	95.4	95.4	95.4	95.4	95.4	95.4	95.4	95.4	95.4
J	95.4	95.4	95.4	95.4	95.4	95.4	95.4	95.4	95.4
K	95.4	95.4	95.4	95.4	95.4	95.4	95.4	95.4	95.4
L	95.4	95.4	95.4	95.4	95.4	95.4	95.4	95.4	95.4
M	95.4	95.4	95.4	95.4	95.4	95.4	95.4	95.4	95.4
N	95.4	95.4	95.4	95.4	95.4	95.4	95.4	95.4 w/O	95.4
O	95.4	95.4	95.4	95.4	95.4	95.4	95.4	95.4	95.4
P	95.4	95.4	95.4	95.4	95.4	95.4	95.4	95.4	95.4
Q	95.4	95.4	95.4	95.4	95.4	95.4	95.4	95.4	95.4
R	95.4	95.4	95.4	95.4	95.4	95.4	95.4	95.4 w/B	95.4
S	95.4	95.4	95.4	95.4	95.4	95.4	95.4	95.4	95.4
T	95.4	95.4	95.4	95.4	95.4	95.4	68.3 d/O	95.4	95.4
U	95.4	95.4	95.4	95.4	95.4	95.4	95.4	95.4	95.4

Table 4. Computational time ranking from the lowest (1) to the highest (9) of the digital systems based on Bessel masks.

#	Masks	Confidence level %
1	B_{NP}	95.4
2	B_{NP}, B_{NN}	95.4
3	B_{NP}, B_{NN}, B_{WP}, B_{WN}	95.4
4	B_{NN}	95.4
5	B_{WP}, B_{WN}	95.4
6	B_{WN}	95.4
7	B_{NN}, B_{WP}	95.4
8	B_{WP}	95.4
9	B_{NP}, B_{WN}	95.4

means that the system has a confidence level of 68.3% due to image X and 95.4 w/X means that the system has a confidence level of 95.4% without considering images X. According to Table 3, the system works excellently and the confidence level of the system reduces as the non-linear factor k goes to one. Hence, based on the results presented in this table to obtain the less computational time the choice of k should be 0.1, 0.2 or 0.3.

Furthermore, an analysis of the efficiency of the system using different arrangements of the masks were done. The system was tested for the non-linear scalar values $k = 0.1, 0.2, \ldots, 0.9$ for the different combinations of the signatures obtained by the masks B_{NP}, B_{NN}, B_{WP} and B_{WN}, and the results are presented in Table 4. The results for all of these combinations showed that the system has an excellent performance, thus it is independent of the non-linear factor k, the issue was the computational cost time. For example, as is shown in Table 3, if you have a $k = 0.4$ the system using diatom D as target will name erroneously some diatoms B as D. But the system identified diatoms B without mistakes, then all images that the system classified as diatoms D will be tested again using the diatom B as the target, hence the system will identify without doubt the diatoms B and the rest are diatoms D, therefore the complete identification is done, but in this way the computational time used will be more. The same idea works for the other cases presented in Table 4, obtaining that the system using the B_{NP} has less computational cost time.

4. Comparison analysis

A comparison of the digital system in Figure 5 (Fourier masks), Figure 9 (Bessel masks) and that developed by Fimbres-Castro, et al. [15] is presented. Also, the vectorial signatures digital system was tested using the database image in Figure 6. The three algorithms have an excellent performance, obtaining each of them a confidence level of at least 95.4%. Also, they show that their responses are independent of the non-linear factor k (Equation (20)). The difference in the three digital systems analysed lies in the time consumption, the algorithm in Figure 5 uses 0.3190 sec, the system in Figure 9 utilizes 0.0780 sec and the vectorial signature employs 0.0923 sec. The times were computed in a MacBook Pro with a processor of 2.3 GHz Intel Core i5 and 8 GB of RAM and memory module 1333 MHz DDR3.

4.1. Noise analysis

To test the performance of the systems based on Bessel masks, Fourier masks and vectorial signatures, the

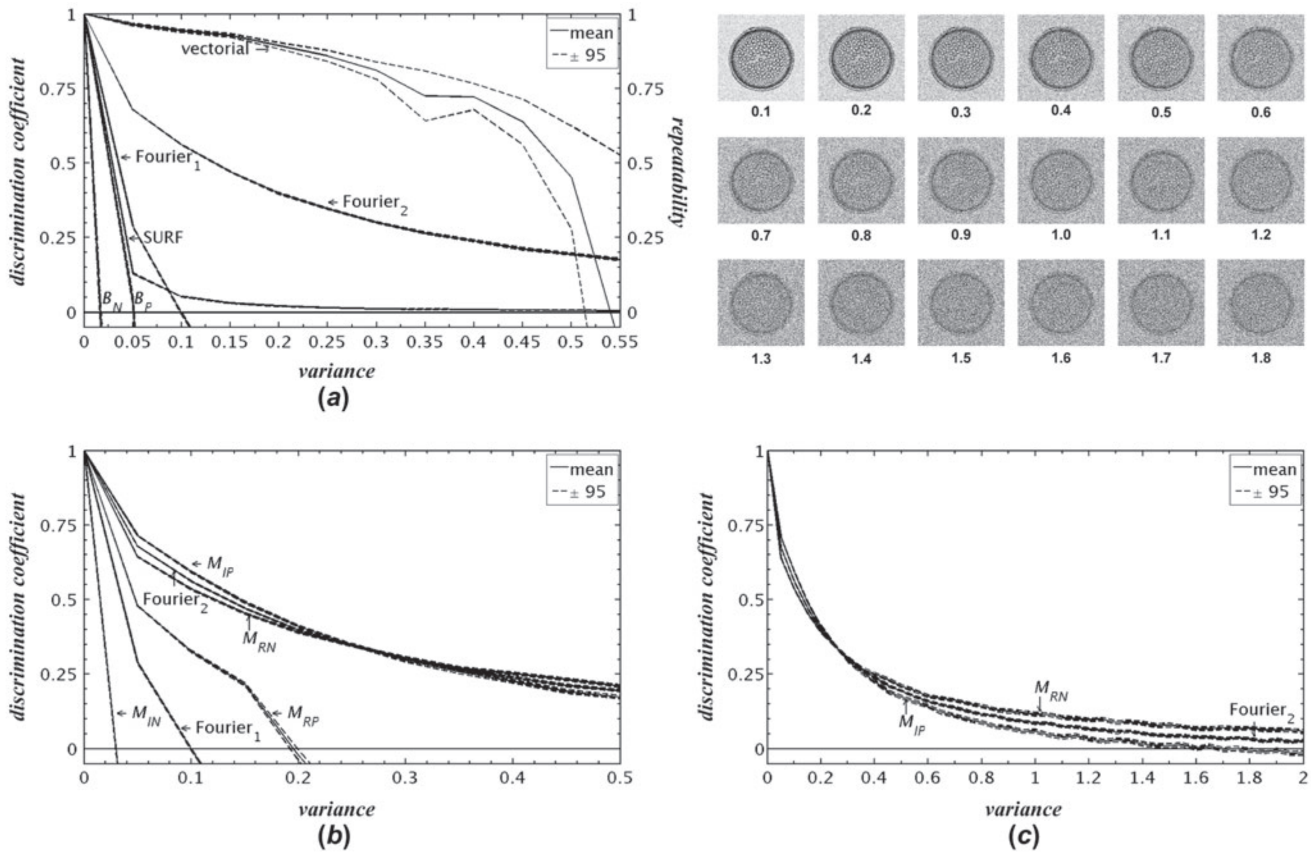

Figure 10. (*a*) The systems under study performance when images have additive Gaussian noise. (*b*) Performance of the four Fourier masks. (*c*) Response of the Fourier$_2$ system.

Table 5. Illumination analysis results with $k = 0.1$. Confidence level (in %).

Diatom	$M_{RP}, M_{RN}, M_{IP}, M_{IN}$	B_{NP}	Vectorial signatures
A	95.4	95.4	95.4
B	95.4	95.4	95.4
C	95.4	95.4	95.4
D	95.4	95.4	95.4
E	95.4	95.4	95.4
F	95.4	95.4	95.4
G	95.4	95.4	95.4
H	95.4	95.4	95.4
I	95.4	95.4	95.4
J	95.4	95.4	95.4
K	95.4	95.4	95.4
L	95.4	95.4	95.4
M	95.4	95.4	95.4
N	95.4	95.4	95.4
O	95.4	95.4	95.4
P	95.4	95.4	95.4
Q	95.4	95.4	95.4
R	95.4	95.4	95.4
S	95.4	95.4	95.4
T	95.4	95.4	95.4
U	95.4	95.4	95.4

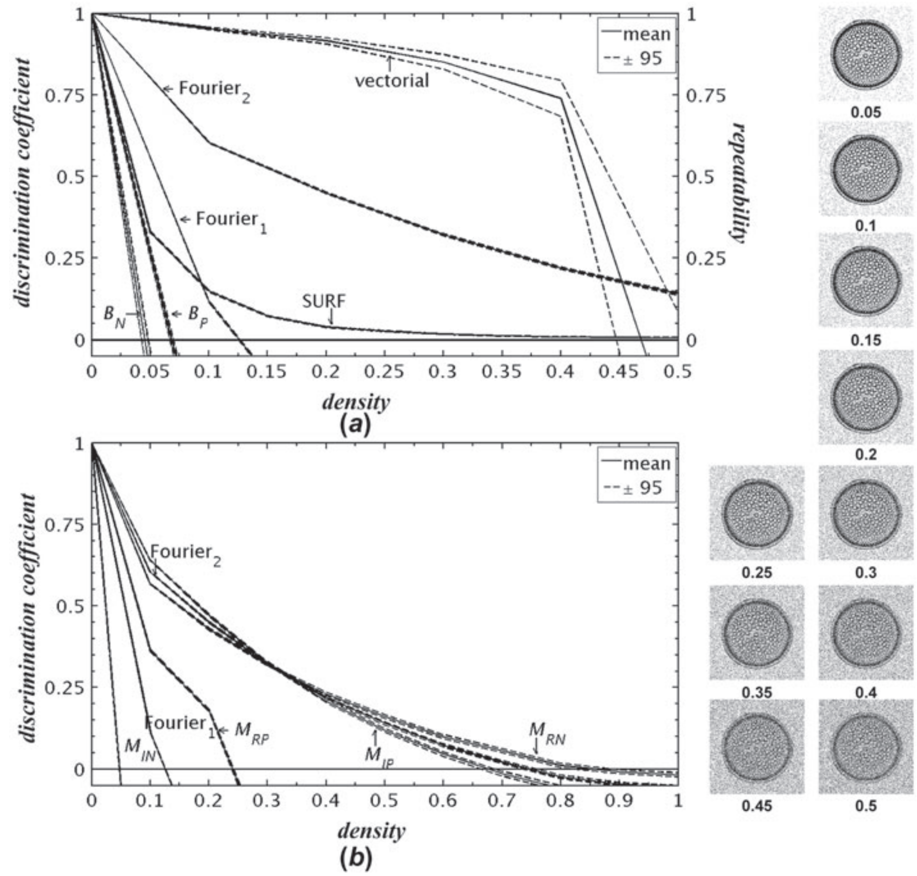

Figure 11. (*a*) The systems under study performance when images have salt and pepper noise. (*b*) Performance of the four Fourier masks.

discrimination coefficient or discrimination capability was used, it is defined as [16],

$$DC = 1 - \frac{\max |C_{NL}(S_T, S_N)|^2}{(P(0))^2}, \tag{23}$$

where $P = |C_{NL}(S_T, S_{TN})|$ and S_T, S_{TN} and S_N are the signatures, respectively, of the target, the target with noise and the background image with noise. For the sake of comparison, the performance of SURF methodology when the images have noise is included, but here the results are given in terms of the repeatability parameter r [17],

$$r = \frac{C(T, PI)}{\text{mean}(N_T, N_{PI})}, \tag{24}$$

where $C(T, PI)$ represents the number of the common detected points in the target T and the problem image PI; N_T and N_{PI} are the number of points detected in T and PI, respectively.

Figure 10(*a*) presents the graphs of the mean of the DC response for the system using the four Fourier masks (Fourier$_1$), the system using the two Fourier masks M_{RN} and M_{IP} (Fourier$_2$), the system using the B_P Bessel mask, the system using the B_N Bessel mask, the vectorial signatures methodology and the repeatability analysis (r values) for the SURF algorithm. The images were altered with additive Gaussian noise of media zero and variance from 0 to 0.55, using 100 images per sample. In Figure 10(*a*) it is shown that the vectorial signatures system has the best response under this kind of noise, followed for the Fourier$_2$ algorithm. The Fourier$_1$, B_P Bessel mask and SURF algorithms have the same performance and the worst results are given by the B_N Bessel mask. Figure 10(*b*) shows that the response of the Fourier$_1$ system reduces its performance due to the contribution of the M_{RP} and M_{IN} masks. When those masks are not being considered in the system, that is Fourier$_2$ methodology, then its performance increases considerably. Moreover, the response of Fourier$_2$ system will be better than the vectorial signatures for variance bigger than 0.5, Figure 10(*c*). The same analysis when performed using salt and pepper noise, obtained the same results as the additive Gaussian noise, Figure 11.

4.2. Illumination

The algorithms by Fouriers masks (Figure 5), Bessels masks (Figure 9) and the vectorial signatures [15] were tested using problem images altered with eight different types of non-homogeneous illumination, Figure 12. The reference

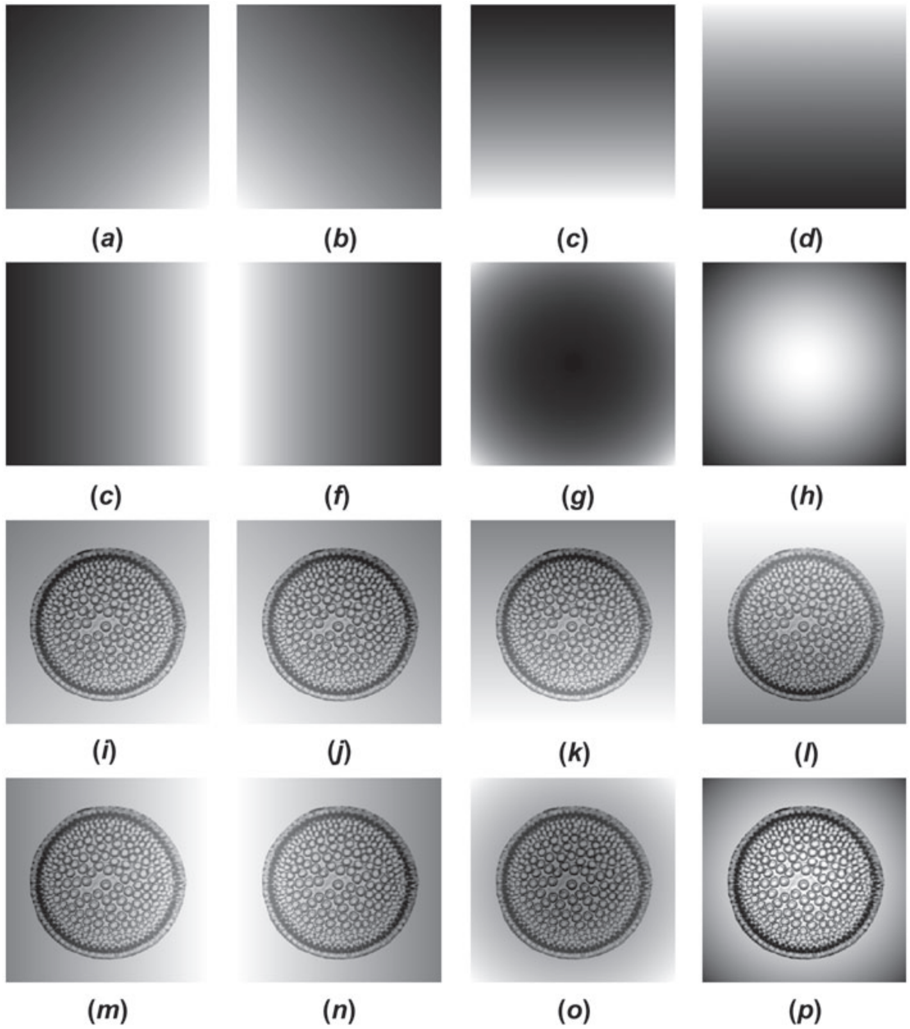

Figure 12. Non-homogeneous illuminations types.

images (Figure 6) were rotated one degree by one degree (until complete the circle) and all of them were altered using the eight different types of non-homogeneous illumination. Hence, the algorithms were proved with 60,480 problem images with different illuminations. Table 5 shows the results of the analysis of the illumination effect in the systems. Basically, the three systems work excellently, hence they are robust in the pattern recognition of images that have non-homogeneous illumination.

5. Conclusions

Using different ways to build the binary rings masks, several digital systems of non-linear correlation invariant to position, rotation, noise and non-homogeneous illumination were presented. The systems were tested using 21 different kinds of fossil diatom greyscale images (real images). The confidence level analysis shows that all systems work efficiently and their responses are k invariant. The computational times analysis yields that the Bessel rings masks algorithms are the best option, but the noise analysis indicates that they are the worst systems for images that have noise and the Fourier system considering only the M_{RN} and M_{IP} masks is a good choice when noise is presented.

Acknowledgements

The grammatical critical review of the manuscript by L.D.I Horacio Padilla Calderón is greatly appreciated. We also thank the unknown reviewers for excellent comments to improve this manuscript.

Funding

This work was partially supported by CONACyT under [grant number 169174].

ORCID

S. Solorza http://orcid.org/0000-0002-7935-6063
J. Álvarez-Borrego http://orcid.org/0000-0002-4038-3435

References

[1] Yuan-Neng, H.; Arsenault, H.H.; April, G. *Appl. Opt.* **1982,** *21,* 4012–4015.
[2] Yuan-Neng, H.; Arsenault, H.H. *Appl. Opt.* **1982,** *21,* 4016–4019.
[3] Arsenault, H.H.; Sheng, Y. *Appl. Opt.* **1986,** *25,* 3225–3229.
[4] Prémont, G.; Sheng, Y. *Appl. Opt.* **1993,** *32,* 3116–3121.
[5] Prémont, G. Conception rapide de filtres d'harmonique circulaire à laide du recuit simulé. Masters Thesis, École des Gradués, Université Laval, Québec, Canada, 1992.
[6] Casasent, D.; Iyer, A.; Ravichandran, G. *Appl. Opt.* **1991,** *30,* 5169–5175.
[7] Vijaya-Kumar, B.V.K.; Teck-Khim, N. *Appl. Opt.* **1996,** *35,* 1871–1878.
[8] Zavala-Hamz, V.A.; Álvarez-Borrego, J. *Appl. Opt.* **1997,** *36,* 484–489.
[9] Solorza, S.; Álvarez-Borrego, J. *Opt. Commun.* **2010,** *283,* 3613–3630.
[10] Álvarez-Borrego, J.; Solorza, S.; Bueno-Ibarra, M.A. *Opt. Commun.* **2013,** *294,* 105–117.
[11] Esparza-Álvarez, M.A. *Variabilidad de la comunidad de diatomeas en los sedimentos de la Cuenca de San Lázaro, Baja California Sur*; México. Tesis de maestría, CICESE, Ensenada, BC, México, 1999.
[12] Hajós, M. *DSSP* **1976,** *5,* 817–883.
[13] Koizumi, I.; Tanimura, Y. Neogene Diatom Boistratigraphy of the Middle Latitude Western North Pacific. In *Deep Sea Drilling Project Leg 86*, Heath, G.R., Burckle, L.H., Eds; Initial Report DSDP, US Gov. Print Office: Washington, DC, 1985. pp 269–300.
[14] Esparza-Álvarez, M.A. *Palecología de sedimentos diatomáceos de la formación Tortugas en el área de Bahía Asunción, Baja California Sur*; México. Tesis de licenciatura, UABC, Ensenada, BC, México, 1995.
[15] Fimbres-Castro, C.; Álvarez-Borrego, J.; Bueno-Ibarra, M.A. *Opt. Eng.* **2012,** *51* (047201), 1–12.
[16] Vijaya-Kumar, B.V.K.; Hassebrook, L. *Appl. Opt.* **1990,** *29,* 2997–3006.
[17] Juan, L.; Gwon, O. *Int. J. Image Proc.* **2009,** *3,* 143–152.